The Astrophysical Journal, 873:65 (15pp), 2019 March 1 https://doi.org/10.3847/1538-4357/ab0361

The Galactic Center: An Improved Astrometric Reference Frame for Stellar Orbits around the Supermassive Black Hole

Shoko Sakai[1], Jessica R. Lu[2], Andrea Ghez[1], Siyao Jia[2], Tuan Do[1], Gunther Witzel[1], Abhimat K. Gautam[1], Aurelien Hees[1,3], E. Becklin[1], K. Matthews[4], and M. W. Hosek, Jr.[5]
[1] UCLA Department of Physics and Astronomy, Los Angeles, CA 90095-1547, USA; shoko@astro.ucla.edu
[2] Astronomy Department, University of California, Berkeley, CA 94720, USA
[3] SYRTE, Observatoire de Paris, Université PSL, CNRS, Sorbonne Université, LNE, 61 avenue de l'Observatoire, F-75014 Paris, France
[4] Astrophysics, California Institute of Technology, MC 249-17, Pasadena, CA 91125, USA
[5] Institute for Astronomy, University of Hawaii, Honolulu, HI 96822, USA
Received 2018 October 13; revised 2019 January 14; accepted 2019 January 17; published 2019 March 5

Abstract

Precision measurements of the stars in short-period orbits around the supermassive black hole at the Galactic Center are now being used to constrain general relativistic effects, such as the gravitational redshift and periapse precession. One of the largest systematic uncertainties in the measured orbits has been errors in the astrometric reference frame, which is derived from seven infrared-bright stars associated with SiO masers that have extremely accurate radio positions, measured in the Sgr A*-rest frame. We have improved the astrometric reference frame within 14″ of the Galactic Center by a factor of 2.5 in position and a factor of 5 in proper motion. In the new reference frame, Sgr A* is localized to within a position of 0.645 mas and proper motion of 0.03 mas yr^{-1}. We have removed a substantial rotation (2.°25 per decade), that was present in the previous less-accurate reference frame used to measure stellar orbits in the field. With our improved methods and continued monitoring of the masers, we predict that orbital precession predicted by general relativity will become detectable in the next ∼5 yr.

Key words: instrumentation: adaptive optics – astrometry – black hole physics – Galaxy: center

Supporting material: machine-readable table

1. Introduction

Over the past 23 years, infrared astrometric and radial velocity data have been gathered for stars orbiting the supermassive black hole (SMBH) at the center of the Galaxy (e.g., Ghez et al. 2008; Gillessen et al. 2009). The diffraction-limited speckle and adaptive optics (AO) observations obtained from the W. M. Keck Observatory and the Very Large Telescope (VLT) have enabled us to characterize the SMBH associated with Sgr A* with unprecedented accuracy. The mass of the SMBH has been estimated to be $(4.02 \pm 0.16) \times 10^6\,M_\odot$ at a distance of 7.86 ± 0.14 kpc (Boehle et al. 2016), which is based on the orbits of two stars, S0-2 and S0-38. In 2018, the star S0-2, with an orbital period of ∼16 yr, passed through closest approach, enabling the first measurement of the gravitational redshift at the Galactic Center (Gravity Collaboration et al. 2018; T. Do et al. 2019, in preparation). Furthermore, in ∼5 yr, the periapse precession predicted by general relativity will be detectable if a stability of the reference frame of ∼0.02 mas yr^{-1} can be achieved (Weinberg et al. 2005). Thus, the need for an improved astrometric reference frame is especially timely.

To make precise and accurate measurements of the stellar orbits around the SMBH, the sky-plane positions of stars around the SMBH are monitored using near-diffraction-limited observations from 8 to 10 m telescopes over many years. There are approximately 3000 stars detected within a 10″ radius of the Galactic Center. However, since nearly all stars are moving within the observed field of view, it is challenging to transform the observed relative astrometry from each observation into a coordinate system that ties multi-epoch observations together.

The astrometric reference frame for the stellar orbits around the Galactic Center that was first used was based on the cluster-rest frame method, in which a set of reference stars were assumed to have no net motion. However, the method was limited by the intrinsic dispersion of the cluster itself, which did not improve with time (Yelda et al. 2010). A better method for establishing an astrometric reference frame in the IR was suggested by Menten et al. (1997) and Reid et al. (2003), and later adapted by Yelda et al. (2010), Ghez et al. (2008), and Gillessen et al. (2009). We utilize radio-emitting SiO maser stars whose positions and proper motions have been determined precisely with respect to the radio source associated with the SMBH, Sgr A*. While Sgr A* is bright at radio wavelengths, it is faint and easily confused in the IR. In contrast, the SiO masers are bright in both the IR and radio and can be utilized as near-perfect astrometric calibrators to bridge the radio and IR astrometric solutions. Because none of the masers is found in the central 10″ region around the Galactic Center (the field of view used for the dynamical study of the SMBH, hereafter referred to as the *central 10″ field*), it is necessary to mosaic the surrounding region of ∼22″, such that the IR astrometric data of seven masers can be extracted. By matching the IR positions of the masers to their corresponding radio positions, the IR astrometric reference frame of the Galactic Center region is established. The presumed dynamical center, the massive black hole at Sgr A*, should then be at the origin of the reference frame and at rest.

The reference frame in this Galactic Center region was previously determined in 2008, based on only three epochs of SiO maser data (Ghez et al. 2008), and later improved in 2010 with six epochs of observations (Yelda et al. 2010). Additional three epochs of maser data (2011–14) were included in the reference frame applied in Boehle et al. (2016). The IR reference frame is constructed with the assumption that Sgr A* is at rest at the origin, determined from the radio astrometric

observations. The precision of the reference frame is then characterized by how well the IR positions of the masers agree with the corresponding radio positions. The objective is to make the agreement as close to zero as possible, and in particular, to ensure that the reference frame does not display any shift with time, which is present in the orbit of S0-2 (e.g., Boehle et al. 2016). Based on the analysis of the astrometric data obtained with NIRC2 at Keck Observatory, Yelda et al. (2010) reported that the reference frame was determined with an accuracy of 0.81 mas in position and 0.17 mas yr^{-1} in proper motion. Based on the observations of eight masers, Plewa et al. (2015) reported an accuracy of ~0.17 mas and ~0.07 mas yr^{-1} in positions and proper motion respectively.

In this paper, we present a new astrometric IR reference frame. Since Yelda et al. (2010), seven additional epochs of maser mosaic data have been obtained. In addition, several modifications were made in various stages of the process of constructing the reference frame, including the use of updated maser proper motions at radio wavelengths, the use of an improved source extraction tool, AIROPA (Anisoplanatic and Instrumental Reconstruction of Off-axis PSFs for AO), to extract astrometric positions on maser mosaic frames, and an improved method of mosaicking lists of stars detected in each epoch of observation. In Section 2, we present the data used to derive the absolute reference frame and how the starlists were created. The method of constructing the astrometric reference frame is detailed in Section 3 and the results are presented in Section 4. The dependence of the reference frame on various methods utilized and modified since (Yelda et al. 2010) is discussed in Section 5. The paper by S. Jia et al. (2018, in preparation) and this paper both focus on the application of the astrometry of NIRC2 data to the study of the stellar orbits around the Galactic Center. This paper concentrates on investigating the stability of the astrometric reference frame reflected by the position and the proper motion of Sgr A^* in IR, while S. Jia et al. (2018, in preparation) examines how to refine the procedure of cross-epoch alignment of astrometric data.

2. Data

2.1. Radio Observations

Maser stars that are detected in both the IR and radio are used to bring the IR stellar positions into an Sgr A^* (radio) rest frame. Reid et al. (2007) presented radio data of masers that were based on five epochs of observations over the period of 1995–2006. In this paper, we use radio positions and proper motions from M. Reid (2018, private communication) that have been updated with two additional epochs of observations.

2.2. Infrared Observations

All the data for the IR observations of SiO masers in the Galactic Center region were obtained using the laser guide-star adaptive optics (LGSAO; van Dam et al. 2006; Wizinowich et al. 2006) facility on the Keck II telescope at the W. M. Keck Observatory. Images were obtained with a near-infrared facility imager (NIRC2; PI: K. Matthews) through the K' ($\lambda_0 = 2.12\,\mu$m, $\Delta\lambda = 0.35\,\mu$m) bandpass. The camera has 1024 × 1024 pixels, with a plate scale of 9.952 mas per pixel (Yelda et al. 2010). Since 2014, the AO system and NIRC2 camera were realigned, and the plate scale was changed to 9.971 mas per pixel (Service et al. 2016). All maser observations were performed with the position angle set to zero. USNO 0600-28577051, which is offset by 9.″4E and 69.″5N from Sgr A^*, served as the tip–tilt star for all of the LGSAO observations. The integration time for each exposure on the Galactic Center (GC) masers was 10.86 s for most epochs, and each comprised 60 co-added 0.181 s exposures in order to avoid saturating the bright masers. The integration time for the central 10″ field is much longer than the maser observations, with each exposure being 28 s, because this field was chosen both to include Sgr A^* and to avoid bright stars that would saturate, such that a longer exposure time was possible.

We used a widely dithered (6″ × 6″) nine-point box pattern with multiple images at each of the nine positions. The number of exposures per dither position changed throughout the 13 years of observations, varying from 3 to 18. Starting in 2012, additional observations of a four-point box pattern (with a smaller dither of 3″ × 3″), with multiple images per dither position, were also obtained in order to average down astrometric errors from unaccounted for field variability in the point-spread function (PSF) due to atmospheric and instrumental aberrations. The data from the four-point box pattern had not been incorporated in any previous analysis. Figure 1 shows the two mosaic patterns covering an area large enough to include seven masers closest to the GC. Figure 1 also shows the positions of the seven masers. The full field of the maser mosaic is 22″ × 22″, corresponding to ~0.88 pc × 0.88 pc at the distance of $R_0 = 8.0$ kpc. A summary of the IR observations and the delivered image quality is given in Table 1. Yelda et al. (2010) included the maser observations from 2005 to 2010. Boehle et al. (2016) then incorporated three additional epochs of maser observations spanning 2011–2013. However, they did not include the inner 2 × 2 dither positions in the construction of the reference frame. The new maser observations added in this paper since Boehle et al. (2016) are indicated by asterisks in Table 1.

2.3. IR Data Reduction

The new NIRC2 data were reduced following the methods described in Yelda et al. (2014). Each NIRC2 frame was sky-subtracted, flat-fielded, corrected for bad pixels, and also corrected for the effects of optical distortion and differential atmospheric refraction (Yelda et al. 2010; Service et al. 2016). The sky background was estimated by taking the median of sky exposures nightly. For optical distortion correction, two independent lookup tables are used. The AO was realigned in 2015, thus the optical distortion correction determined by Yelda et al. (2010) is applied for the data taken prior to 2015, while the correction by Service et al. (2016) is used for data taken in 2015 and later.

For each dither position, a bright isolated star is selected whose position is used to register and mosaic together multiple exposures. The final image for each dither position was created by including only those frames having an FWHM less than 1.25 times the smallest FWHM value measured for the dither position. If the number of exposures per dither position was only 3, which was the case for most of the earlier observations, and for the 2 × 2 dither pattern for all years except 2017, all exposures were used to create the final image at each dither position. Furthermore, the frames for each dither position were subdivided into three independent subsets. Each subset consisted of frames of similar FWHM and Strehl ratio. The images in each subset were then combined to make three "submap" images for each dither position. The standard

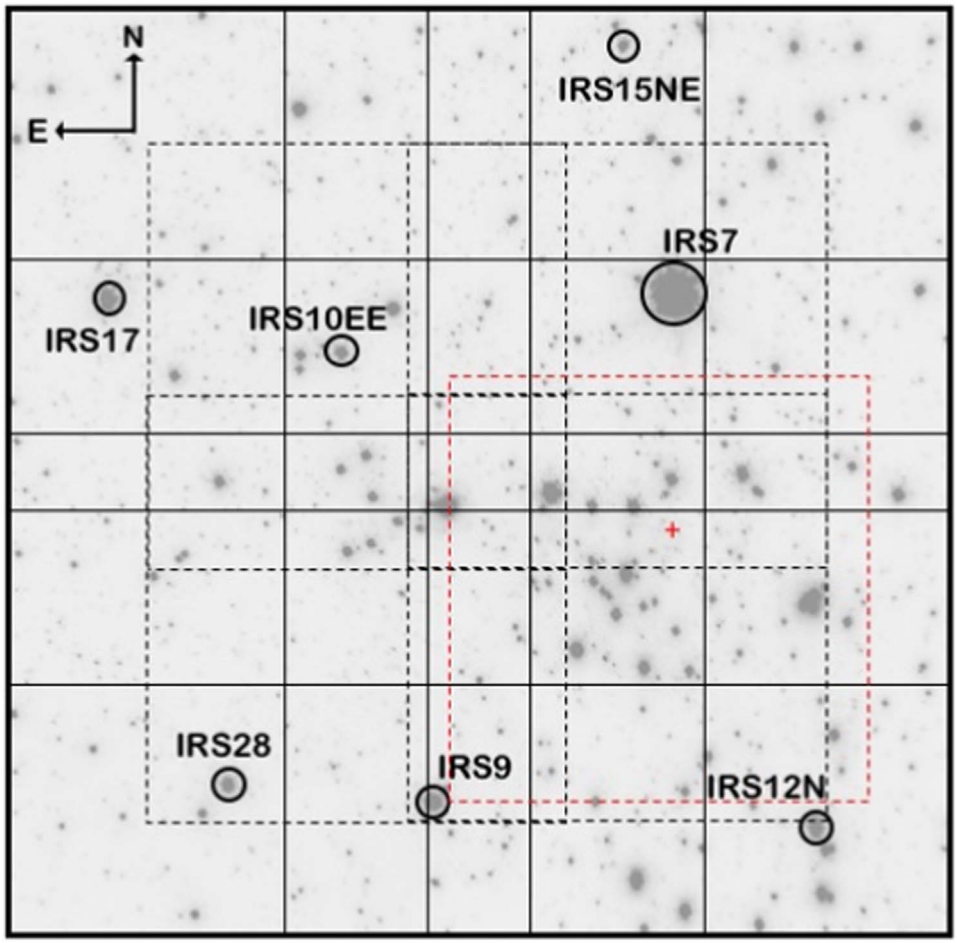

Figure 1. NIRC2 K' image of the Galactic Center showing the maser positions in solid black circles. The 3 × 3 dither positions of the mosaic are shown by solid-line squares, and the 2 × 2 dither positions by dashed lines. The position of Sgr A* is indicated by a red cross and the central 10″ image used for the orbit study is shown by dashed red box. Each NIRC2 field is 10″ × 10″. The entire maser mosaic field is 22″ × 22″.

deviation of measured positions over the three submap images was used for initial estimates of astrometric uncertainties. The positional uncertainties estimated from submaps range from 0.06 pixels (∼0.6 mas) on average for stars brighter than $K' = 12$ up to ∼0.1 pixel for stars with $14 < K' < 15$. The signal-to-noise ratio (S/N) is ∼10,000 for $K \sim 12$ stars. For fainter $K \sim 14$–15 mag stars, the S/N is ∼4000. The astrometric uncertainties are larger, in general, in the maser mosaic data than in the central 10″ data. This is because the central 10″ observations are much longer and deeper; the central 10″ data comprise hundreds of frames, each with a total exposure time of 2.8 s × 10 co-adds.

2.4. Starlists

With the fully reduced dithered images, the next step is to make a master starlist consisting of values of stellar positions and proper motions. Instead of creating a mosaicked image, we first extract stellar positions from the combined images at each dither position and then mosaic the starlists as described below (Yelda et al. 2014).

First, the photometry and astrometry were extracted on each dither position for each epoch using the AIROPA package developed by the UCLA Galactic Center group (Witzel et al. 2016), based on the PSF-fitting code StarFinder (Diolaiti et al. 2000). This package was designed to take atmospheric turbulence profiles, instrumental aberration maps, and images as inputs and then fit field-variable PSFs to deliver improved photometry and astrometry on crowded fields. Although a single PSF was applied for the data used in this paper, the PSF extraction benefited from a much improved method because AIROPA uses improved StarFinder subroutines. For each dither position, we selected ∼30–60 isolated stars spread throughout the NIRC2 field of view, which are combined to create a single PSF model. This PSF is then used to extract positions and fluxes using PSF-fitting methods. A similar analysis is performed on the three submap images as well.

The starlists from all the dither positions were then combined together to create one master starlist for each epoch, by following the iterative steps described below. (1) First, we use the positions of stars presented in Table 6 of Boehle et al. (2016) (hereafter GC starlist) as a starting point to launch an iterative process of mosaicking together starlists from individual mosaic positions to create a combined single master starlist for each epoch of NIRC2 observation. The GC starlist comprises ∼830 stars, spanning the same region as the maser frames. The positions given in arcseconds and proper motion values given in mas yr^{-1} had been determined from the previous construction of the reference frame, in which accelerating sources were excluded (see Section 3 for details). An initial guess for the positions of stars in any given epoch can then be estimated using the values given in this GC starlist.

Table 1
Summary of GC Maser Mosaic Images

Date (UT)	$t_{exp,i}$ × Co-add (s)	N_{exp}[a] per dither position	K'_{lim}[b] (mag)	FWHM[c] (mas)	Strehl[d]	N_{stars}[e]	σ_{pos}[f] (mas)
2005 Jun 30	0.181 × 60	2 (3 × 3)	15.18	60.1	0.32	1143	1.25
2006 May 3	0.181 × 60	3 (3 × 3)	15.57	61.2	0.28	1242	1.10
2007 Aug 12	0.181 × 60	3 (3 × 3)	15.66	56.6	0.29	1474	1.15
2008 May 15	0.181 × 60	3 (3 × 3)	15.92	53.5	0.35	1861	1.05
2009 Jun 28	0.181 × 60	9 (3 × 3)	16.12	63.5	0.26	2274	1.10
2010 May 4	0.181 × 10	18 (3 × 3)	15.52	67.6	0.25	1110	1.25
2011 Jul 20	0.181 × 60	6 (3 × 3)	15.87	63.2	0.27	2033	1.20
2012 May 15	0.181 × 60	6 (3 × 3) + 3 (2 × 2)[g]	15.82	55.9	0.34	2226	1.10
2013 Jul 2	0.181 × 60	18 (3 × 3) + 4 (2 × 2)[g]	16.11	59.1	0.31	2745	1.20
2014 May 20	0.181 × 60	18 (3 × 3)[g] + 3 (2 × 2)[g]	16.14	65.8	0.24	2586	1.20
2015 Jul 10	0.181 × 60	18 (3 × 3)[g] + 3(2 × 2)[g]	16.44	65.4	0.27	3216	1.20
2016 May 15	0.181 × 60	18 (3 × 3)[g] + 3 (2 × 2)[g]	15.99	80.1	0.19	2329	1.30
2017 May 5	0.181 × 60	18 (3 × 3)[g] + 18 (2 × 2)[g]	16.51	58.9	0.31	3265	1.20

Notes.
[a] Number of exposures per dither position. The dither pattern is indicated in brackets.
[b] K'_{lim} is the magnitude at which the cumulative distribution function of the observed K' magnitudes reaches 90% of the total sample size.
[c] Mean FWHM of stars detected in each epoch.
[d] Mean Strehl ratio of stars detected in each epoch.
[e] Number of stars detected in each epoch.
[f] Mean total astrometric measurement error.
[g] Maser data that had not been used in previous reference frame analyses.

Matching and transforming a starlist from one dither position to the GC starlist is performed by fitting a third-order, 20-parameter (10 in each dimension) polynomial to the positional offsets of ∼100 stars. The third-order fit was used in order to take care of the time-dependent residuals, likely stemming from the variable PSF, that were present after the corrections for geometric distortion (Yelda et al. 2010; Service et al. 2016) were applied. More details are given in the Appendix. This transformation step was iterated as each iteration added more stars, and thus a better transformation was calculated. This matching procedure is repeated for all observed dither positions.

(2) Now we have either 9 or 13 transformed starlists in arcseconds for each epoch, depending on how many dither positions were observed (see Table 1). Next, all the starlists for a given epoch are combined together to create one master list, spanning ∼22 × 22 arcsec per epoch. For stars found in the overlap regions, the mean positions were used, with the standard deviation of the mean used as the positional uncertainties. The typical astrometric uncertainties in the mosaicked image range from ∼0.05 mas for stars brighter than $K \sim 12$ mag up to ∼2 mas for $K \sim 15$ mag. For comparison, the mean uncertainties in the central 10″ data, which are much deeper than the maser mosaic observations, are around ∼0.09 mas.

(3) The newly created mosaicked master list is used as the reference starlist and steps 1 and 2 above are repeated six times. After three or four iterations, the standard deviation of the match between the reference starlist and the mosaicked starlist for each mosaic position converges to <1 mas (∼0.1 pixel).

The accuracy of the stellar positions after the first iteration in step 2 is 1.7 mas in the east and 2.2 mas in the north, which decrease to 1.3 and 1.8 mas for subsequent iterations. The uncertainty in the N/S direction is worse than in the E/W. This is likely due to the position of the tip–tilt star located NNE of the entire maser mosaic field, which causes the PSF to be elongated in that direction and leads to poorer measurement precision. The numbers of stars and mean position uncertainties for each epoch are listed in Table 1.

3. Radio Sgr A* Rest Reference Frame

3.1. Constructing the IR Astrometric Reference Frame

The goal of constructing the IR astrometric reference frame is to produce a set of secondary astrometric standard stars whose proper motions are linear and well measured. Their positions at a given epoch can then be used to define the coordinate system for that epoch. Stellar positions from multiple epochs can then be aligned together in the IR reference frame to derive the proper motions and accelerations of those stars in the region close to Sgr A* for determinations of orbits.

We start out with 13 starlists, each produced from one epoch of NIRC2 mosaic observations of SiO masers by following the procedure described in the previous section. The 13 sets of data span 13 years from 2005 to 2017. First, the seven maser positions from the individual starlist per epoch need to be transformed to their radio positions propagated to the corresponding epoch. The radio maser positions are calculated from the proper motion measurements given by M. Reid (2018, private communication).

We note that the intrinsic size of Sgr A* is less than 1 au, corresponding to ∼0.13 mas at the distance of the Galactic Center (Reid & Brunthaler 2004). Thus the uncertainty in the reference frame resulting from the error in the size measurement of Sgr A* is minimal. In addition, the position of Sgr A* in the radio is determined with an uncertainty of ∼1 mas. We also note that Sgr A*'s proper motion is -3.151 ± 0.018 mas yr^{-1} and 5.547 ± 0.026 mas yr^{-1} in the east and south directions respectively (Reid & Brunthaler 2004), with respect to background QSOs. However, the reference frame

being derived in this paper is based on the assumption that Sgr A* is at rest. In other words, our frame is relative to Sgr A*.

Compared to the radio data used in Yelda et al. (2010), one or two additional astrometric points for each maser were included in the derivation of proper motions. For the radio positions and proper motions, it is assumed that Sgr A* is at the Galactic Center and at rest. Thus ideally the same assumption holds for the IR reference frame. The positional uncertainties in the propagated radio measurements vary from 0.3 to 5 mas depending on the maser, with a mean of ∼1.35 mas. For the alignment of IR and radio positions of the masers, six independent parameters were used (translation, rotation, and pixel scale independently in the east and north, to first order). The transformed IR starlist is now in the astrometric reference frame in which the Sgr A* radio source is at rest. This exercise was repeated for all 13 epochs, resulting in a set of 13 starlists that are all in the same radio astrometric reference frame.

The errors in the transformation of the IR positions to the radio Sgr A* rest frame in each epoch were calculated by a jackknife method, in which one maser was dropped from the alignment at a time. The standard deviation of seven "drop-one-maser" cases for each star was adopted as the positional uncertainty. The total astrometric uncertainty for a star's position in every epoch is estimated by combining the positional, alignment, and distortion correction errors. For the error in distortion correction, the average value of 1 mas, as derived by Yelda et al. (2010) and Service et al. (2016), was added to the astrometric errors in the east and north.

Next, the proper motions for all astrometric secondary standard stars are determined. The 13 epochs of starlists are in a common coordinate system and are cross-matched to identify each star across all epochs. The proper motions are then determined by fitting a linear velocity model to each star's positions over time. The proper motion errors were estimated using a jackknife resampling method. Out of ∼3900 stars detected in the entire maser mosaic field, 1008 stars were detected in at least 12 of the 13 epochs. For a star to be included in the secondary astrometric standard starlist, it needed to meet the following conditions: magnitude of proper motion in both the x and y directions $<10\,\mathrm{mas\,yr^{-1}}$, uncertainties in the x and y proper motions $<0.2\,\mathrm{mas\,yr^{-1}}$, and both χ^2 values in x and y directions for proper motion fits less than 20, to exclude accelerating stars. The final secondary standard starlist contains 748 stars. Table 2 lists the properties of secondary IR astrometric standard stars.

4. Results

The quality and stability of the astrometric reference frame are quantified in a number of ways. First, Table 3 shows a summary of how well the IR and radio SiO maser positions and proper motions agree. The columns of the table are: (1) name of the maser used; (2) K' magnitude; (3) total reduced χ^2 values for proper motion fits; (4) the average time of the IR positional measurements; (5) the epoch at which the positional difference is expected to have the smallest uncertainty for each maser, estimated using Equation (3) in Yelda et al. (2010); (6) and (7) the mean difference in the east and north directions between the measured IR and predicted radio positions. The IR formal uncertainties are dominated by the average distortion error of 1 mas which is added in quadrature; and (8) and (9) differences between the IR and radio proper motions. In the last row, the weighted averages of these residuals are tabulated. For a perfect reference frame, these residuals should be zero in both position and velocity; thus they are useful for estimating the stability of the reference frame and how well the positions and proper motions of Sgr A* are determined in the IR reference frame.

The comparisons listed in Table 3 show that the position of Sgr A* in the IR is known to within 0.458 mas and 0.455 mas in the east and north directions, respectively, in the year 2008.5. The velocity of Sgr A* in the IR reference frame is estimated with an accuracy of $\sim 0.03\,\mathrm{mas\,yr^{-1}}$. The results of how well the IR maser positions agree with the radio positions are also shown in Figure 2. For each maser, the observed IR positions are plotted as a function of time in the top panels, with the fitted IR velocities overplotted. The coordinates are defined such that X increases to the east and Y increases to the north. Also shown by red dashed lines are radio velocities provided by M. Reid (2018, private communication). In the bottom panels, the residuals of the IR observed points with respect to the radio velocities are plotted for each maser. The error bars show the IR positional uncertainties while the red shaded region represents the uncertainty in the radio velocities. The mean weighted rms of the IR fits to the radio velocities is $0.35\,\mathrm{mas\,yr^{-1}}$.

We note that when comparing the positions of the maser sources in the IR and radio, the intrinsic source positions may differ. SiO maser emission originates in the extended atmospheres of late red giants and supergiants. The emission comes from a radius of ∼4 au typically, corresponding to ∼0.5 mas at the distance of the Galactic Center (Reid et al. 2007); and the SiO emission may not be symmetrically distributed. The resulting systematic difference between the centroid of the maser emission and the photospheric centroid should be significantly less than this. The radio centroid of the emission typically has a measurement uncertainty of about ±0.5 mas (Reid et al. 2007), which is larger than the expected systematic uncertainty. Even for the largest maser in our sample, IRS 7, its photospheric diameter is estimated to be 2.6 mas (Pott et al. 2008), with a ratio of molecular envelope radius to the photospheric size of ∼2–2.2 (Danchi et al. 1994; Ohnaka et al. 2005; Wittkowski et al. 2007; Perrin et al. 2015). We expect very little systematic offset in the final position of Sgr A*, since seven masers are used in establishing the reference frame, and thus any uncertainties arising from the radio–IR mismatch of their centroids should be random. It is very unlikely that in all seven masers the SiO emission ring is skewed or asymmetric in the same direction.

Because the velocity-fit χ^2 values are used to select the astrometric standard stars, we need to be certain that the errors are estimated correctly. If they are underestimated, then more stars would be excluded based on their inaccurately estimated large χ^2 values, even though these stars are not likely accelerating. Overestimated errors would, on the other hand, lead to truly accelerating sources being included in the astrometric standard starlist, as their χ^2 values are underestimated. Examining the χ^2 distribution as shown in Figure 3, the astrometric errors seem to be estimated accurately because they follow the χ^2 distribution of the corresponding degree of freedom, which is shown by the solid line.

We have also examined the distribution of the directions of proper motion vectors as shown in the left panel of Figure 4. The magnitudes and directions of all stars used as secondary

Table 2
Secondary IR Astrometric Standard and PSF Stars in the Galactic Center

Name	K' (mag)	$T_{0,\mathrm{IR}}$ (yr)	Radius (arcsec)	ΔR.A. (arcsec)	$\sigma_{\mathrm{R.A.}}$[a] (mas)	ΔDecl. (arcsec)	$\sigma_{\mathrm{Decl.}}$[a] (mas)	$v_{\mathrm{R.A.}}$ (mas yr^{-1})	$\sigma_{v\mathrm{R.A.}}$[b] (mas yr^{-1})	$v_{\mathrm{Decl.}}$ (mas yr^{-1})	$\sigma_{v\mathrm{Decl.}}$[b] (mas yr^{-1})	Astrometric Standard[c]	PSF Star[d]
S0-6	14.3	2010.86	0.36	0.0154	0.2000	−0.3563	0.2200	−5.057	0.051	3.065	0.075	Y	
S0-11	15.4	2011.37	0.49	0.4896	0.2200	−0.0657	0.4300	−3.637	0.033	−2.530	0.080	Y	
S0-7	15.4	2012.37	0.54	0.5268	0.2600	0.1002	0.2900	5.711	0.052	0.727	0.069	Y	
S0-13	13.5	2011.00	0.69	0.5575	0.2000	−0.4073	0.2400	1.874	0.048	3.136	0.063	Y	
S0-12	14.4	2011.53	0.69	−0.5497	0.2200	0.4198	0.2100	1.060	0.045	3.399	0.055	Y	C_SW
S0-31	15.1	2012.08	0.73	0.5810	0.4400	0.4470	0.8200	6.377	0.116	0.885	0.273	N	C_SW
S0-14	13.9	2011.40	0.81	−0.7533	0.2200	−0.2888	0.2800	2.514	0.051	−1.446	0.082	Y	C_NW, C_SW, W
S1-5	12.7	2011.08	0.94	0.3142	0.2400	−0.8833	0.1800	−3.671	0.067	4.304	0.053	Y	

Notes.
[a] Positional errors include errors due to centroiding, alignment, and residual distortion (1 mas), but do not include the error in position of Sgr A* (0.01 mas and −0.16 mas in R.A. and decl. respectively).
[b] Velocity errors do not include the error in velocity of Sgr A* (0.018 mas yr^{-1} and 0.004 mas yr^{-1} in R.A. and decl. respectively.
[c] Indicates whether the star is a secondary astrometric standard.
[d] Indicates for which mosaic field the star was used to create a PSF.

(This table is available in its entirety in machine-readable form.)

Table 3
Astrometry of SiO Masers

Maser	K' (mag)	$\tilde{\chi}^2$[a]	T_0[b] IR (yr)	T_0[c] IR + Radio (yr)	R.A. Position[d] [IR − Radio] (mas)	Decl. Position[d] [IR − Radio] (mas)	R.A. Velocity[e] [IR − Radio] (mas yr^{-1})	Decl. Velocity[f] [IR − Radio] (mas yr^{-1})
IRS 9	9.063	0.17	2011.1	2010.2	0.139 ± 1.007 ± 0.219	0.313 ± 1.019 ± 0.375	0.073 ± 0.027 ± 0.043	0.088 ± 0.042 ± 0.074
IRS 7	7.658	0.52	2011.0	2009.4	1.557 ± 1.044 ± 5.001	2.767 ± 1.044 ± 5.002	0.034 ± 0.076 ± 0.122	−0.829 ± 0.067 ± 0.225
IRS 12N	9.538	0.03	2011.1	2006.6	−0.253 ± 1.001 ± 0.210	−0.199 ± 1.003 ± 0.409	−0.022 ± 0.009 ± 0.027	0.000 ± 0.017 ± 0.052
IRS 28	9.328	0.12	2011.6	2011.2	0.328 ± 1.006 ± 0.588	0.231 ± 1.016 ± 0.428	−0.080 ± 0.024 ± 0.128	−0.089 ± 0.036 ± 0.099
IRS 10EE	11.270	0.11	2011.1	2008.8	0.106 ± 1.006 ± 0.173	−0.651 ± 1.012 ± 0.196	0.026 ± 0.024 ± 0.024	−0.002 ± 0.037 ± 0.028
IRS 15NE	10.198	0.03	2011.0	2005.0	0.118 ± 1.002 ± 0.320	0.268 ± 1.003 ± 0.307	−0.009 ± 0.014 ± 0.040	0.021 ± 0.016 ± 0.038
IRS 17	8.910	0.24	2011.1	2007.9	−1.457 ± 1.005 ± 1.855	0.331 ± 1.023 ± 1.167	−0.356 ± 0.012 ± 0.603	0.268 ± 0.038 ± 0.214
Weighted Average[e]		0.17		2008.5	0.015 ± 0.458	0.033 ± 0.455	0.005 ± 0.018	0.004 ± 0.025

Notes. Infrared (first) and radio (second) formal uncertainties are reported for each maser's position and velocity. Average distortion errors ($\sigma \sim 1$ mas) for each maser are added in quadrature to the infrared formal uncertainties. X and Y increase to the east and north, respectively.

[a] $\tilde{\chi}^2$ is the average of the X and Y χ^2 per degree of freedom.

[b] weighted average time of IR measurements.

[c] Average T_0 from both IR and radio measurements weighted by velocity errors.

[d] Positional offsets computed for the common epoch of 2008.6. The first and second uncertainties are those in the IR and radio respectively.

[e] Velocity offsets computed for the common epoch of 2008.6. The first and second uncertainties are those in the IR and radio respectively.

[f] Weighted average and error in the weighted average are reported for all columns except the $\tilde{\chi}^2$ and T_0 columns, where we report the average.

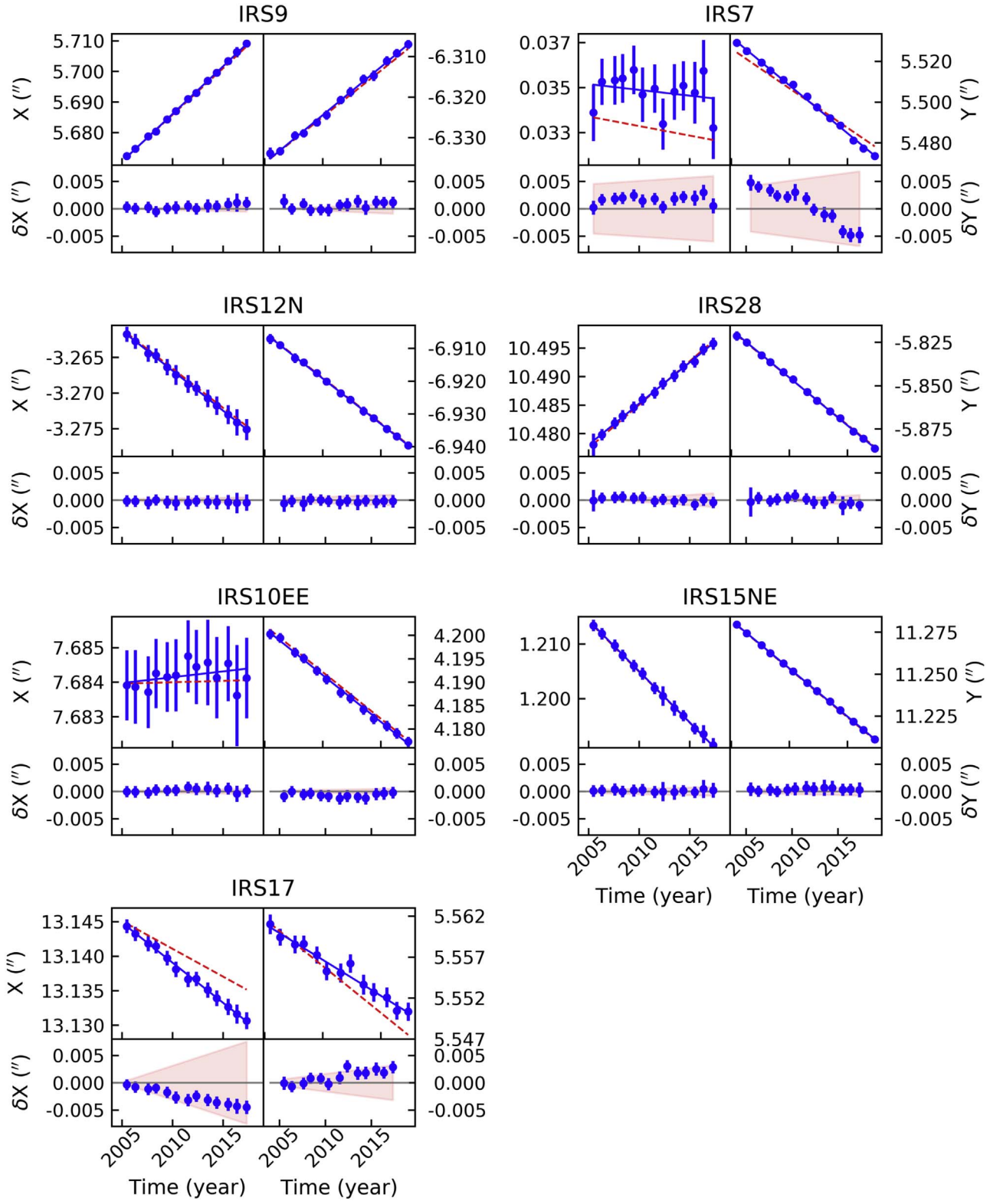

Figure 2. The positions over time for the seven masers, one per panel, in both the X/east (top left) and Y/north (top right) directions. The fits to the IR and radio proper motions are overplotted as blue and red lines, respectively. The 1σ error limits in the radio proper motions are shown by the red shaded regions. In the bottom panels, the residuals of the IR observed points with respect to the radio velocities are plotted for each maser. The error bars show the IR positional uncertainties while the red shaded regions represent the uncertainty in the radio velocities.

astrometric standard stars are plotted here, with seven masers highlighted by thicker blue arrows. There is no obvious pattern in the distribution of these vectors; they are randomly spread, suggesting that there is likely no underlying directional bias in the method used to derive proper motion measurements of stars in the GC region.

In the middle panel of Figure 4, the proper motion distributions in the east and north directions are shown in the

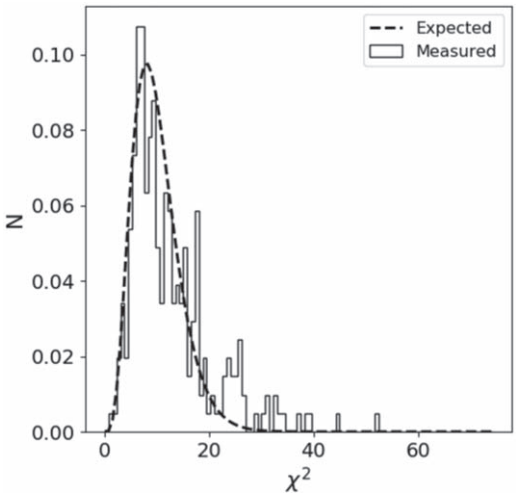

Figure 3. Distribution of χ^2 values of velocity fits to all the stars found on the maser mosaic field, before applying cutoffs to create the list of secondary astrometric standard stars. The expected distribution is that of a corresponding χ^2 distribution for the degree of freedom of 10, for stars found in at least 12 out of the total of 13 epochs. For a star to be selected as a secondary astrometric standard star, its χ^2 value in both $V_{\rm R.A.}$ and $V_{\rm decl.}$ must be less than 20.

top and bottom panels, respectively. Skewness in the velocity distribution is observed, especially in the N/S direction. This is likely due to the fact that the early-type stars that comprise the clockwise disk of stars are included in the sample. Outside a 7″ radius from Sgr A*, although the skewness in the velocity distribution decreases slightly, there are clearly more stars with positive velocities than negative velocities. Furthermore, in the right panels of Figure 4, the distribution of proper motion errors is shown. The velocity errors in the N/S direction are slightly larger than those in the E/W direction on average. It was also already shown that the agreement between the IR and radio proper motions in the *Y* direction is not as well constrained as it is in the east direction, as seen from the average values listed in Table 3. As mentioned above in Section 2.4, this is likely due to the fact that the tip–tilt star used for the LGSAO observations is to the northeast of the maser mosaic NIRC2 fields, resulting in the larger uncertainties in the geometric distortion correction in the north direction. The velocity distributions are shown in the middle panel of Figure 4. The mean position and velocity of 286 stars within 7″ are zero within 1σ. The velocities of the same set of stars within 7″ are also zero.

4.1. Comparison with Previous Works

In Figure 5, the stability of the reference frame derived in this paper is compared with those of previously published results. In Yelda et al. (2010), six epochs of maser data were used, instead of 13 used in this paper. When comparing the stability of the reference frame, the uncertainty in distortion correction of 1 mas that was added in the formal IR error (see Table 3) is subtracted, because we would like to focus on the improvement made in the methods used to construct the reference frame. Without this uncertainty, the reference frame of Yelda et al. (2010) yields uncertainties in Sgr A*'s position of 0.319 mas and 0.382 mas in the east and north directions respectively. In this paper, Sgr A*'s position is estimated with uncertainties of 0.122 mas and 0.157 mas in the east and north directions respectively, indicating that the reference frame has been improved by a factor of ∼2.5 in position. The uncertainties in the proper motions of Sgr A* in the IR reference frame are 0.02 and 0.03 mas yr^{-1} in the east and north directions, respectively, compared to 0.09 and 0.14 mas yr^{-1} reported by Yelda et al. (2010). The orbital analysis of Boehle et al. (2016) was based on a reference frame that had three epochs of maser observations (2011–13) in addition to those used in Yelda et al. (2010). The uncertainties in the proper motions in the east and north directions of Sgr A* were 0.056 and 0.060 mas yr^{-1} respectively.

Using the NACO imager on VLT, Plewa et al. (2015) reports a stability of ∼0.17 mas in position and ∼0.07 mas yr^{-1} in velocity. Their analysis used eight masers because their mosaicked field covered 42 arcsec × 42 arcsec. However, their maser sample did not include IRS 7. IRS 7 is a supergiant and its SiO maser features originate from a much larger maser emission region than the other masers used (Reid et al. 2003) by a factor of ∼2, which is reflected in larger uncertainties in the star's radio positions and proper motions. To see how much effect this one star has on the IR reference frame, we construct the reference frame without IRS 7. Excluding IRS 7, we obtain combined positional and velocity uncertainties of 0.17 mas and 0.031 mas yr^{-1} respectively. The velocity stability of our sample of six masers, without IRS 7, is still a factor of 2 better than the one reported by Plewa et al. (2015). This is because IRS 7 has less influence on the overall reference frame due to the very large errors assigned to its radio velocities. The maser sample used by Plewa et al. (2015) also had one less epoch of the radio observations. Furthermore, their IR observations included data through 2013, while our IR data extend four additional years. As explained in Section 5, the IR data and the method used to create the reference frame presented in this paper were modified significantly compared to those used in Yelda et al. (2010). The comparison of the reference frame of Boehle et al. (2016) with that of Plewa et al. (2015) is likely more appropriate, because both use the maser data through 2013.

5. Discussion

We have presented an improved astrometric reference frame that utilizes 13 years of IR observations of radio-emitting SiO masers in the vicinity of the Galactic Center. Since our previous work in Yelda et al. (2010), several modifications have been made in the construction of the reference frame including: (i) using 13 epochs of maser data (2005–2017) instead of six epochs (2005–2010) used by Yelda et al. (2010); (ii) using an improved PSF-fitting package, AIROPA, instead of StarFinder v1.6 (Diolaiti et al. 2000) used in Yelda et al. (2010); (iii) using a new method to mosaic 9 or 13 dither positions for each epoch of observations. Yelda et al. (2010) stitched together one field at a time, building up the starlist by one position after another. Instead, we transformed all dither positions simultaneously by transposing each list to the reference master starlist; (iv) applying a six-parameter fit to transform the IR maser positions to the radio Sgr A* rest reference frame, while Yelda et al. (2010) used a four-parameter fit; and (v) using an updated set of radio maser positions and proper motions (M. Reid 2018, private communication).

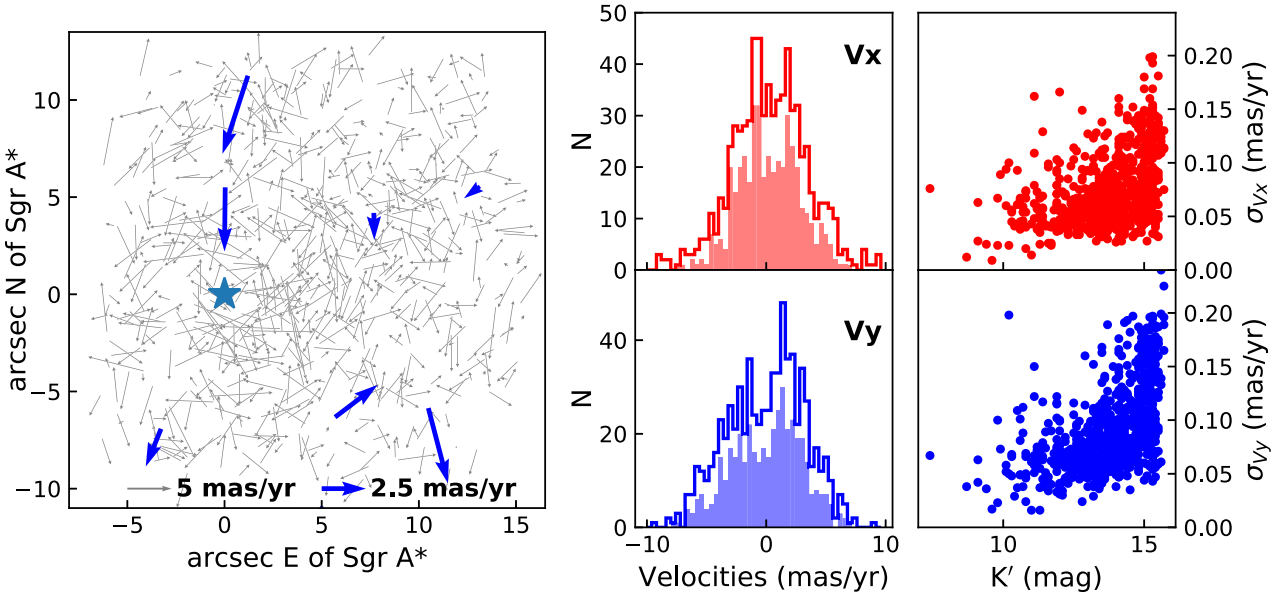

Figure 4. Left: the distributions of proper motions on the sky. Seven masers highlighted with blue arrows and the position of Sgr A* marked by a star are shown. There is no obvious pattern seen in the distribution; the proper motion vectors appear to be directed randomly. Middle: the number distributions of proper motions. Skewness is seen in the *Y* direction, which is likely due to rotation along the Galactic plane seen preferentially on the near-side of the Galactic Center. The unshaded histograms correspond to the distributions of all stars, while the shaded histograms show those of stars outside the 7″ radius. Right: the distributions of proper motion uncertainties. The uncertainties in the *Y* direction are worse for a given magnitude. This is likely due to the position of the tip–tilt star used in the NIRC2 observations.

5.1. Dependence on the Number of Epochs of Observations

The stability of the reference frame improved by a factor of ∼5 compared to that of Yelda et al. (2010), to which the change in each one of the above five processes contributed. Of the five, the number of epochs of maser mosaic observations has had the most significant effect on the improvement of the stability of the reference frame . If we were to build the reference frame using seven epochs of data spanning the years 2005–2011, with all other conditions remaining the same, the uncertainties in the velocities in the reference frame would increase to 0.023 and 0.043 mas yr^{-1} for $V_{\rm R.A.}$ and $V_{\rm decl.}$ (from 0.018 and 0.025 mas yr^{-1}). However, if we used seven epochs spread over 13 years from 2005 through 2017, skipping every other year, then the velocity uncertainties would remain similar (0.021 and 0.025 mas yr^{-1}). Thus it is not just the number of epochs that is important in creating a stable reference frame, but the range of dates of observations. The longer the time baseline, the more accurate the reference frame becomes. We attribute this to the improved precision and accuracy of the proper motions of the secondary astrometric stars.

5.2. Stability of the Reference Frame Based on the Choice of Masers

The IR astrometric reference frame is stable within 0.03 mas yr^{-1} (Table 3). However, this is based on the radio observations of proper motions of seven SiO masers only. There are 16 masers that can be used potentially to create the radio Sgr A* rest reference frame (Reid et al. 2003). However, given the field of view of NIRC2 and the feasibility of telescope scheduling, we have only been able to mosaic together a field large enough to cover the seven masers closest to Sgr A*. Because of dependence of this field on a small number of astrometric anchor points, we examine in this section how sensitive the global parameters of the SMBH are to the selection of masers.

We have applied a jackknife resampling method, in which one maser at a time is excluded from the construction of the reference frame. The proper motions of secondary astrometric standard stars derived from the radio positions of the remaining six masers change systematically. As mentioned above, the positional uncertainties of secondary astrometric stars are calculated by taking the average of seven drop-one-maser cases, with the assumption that this does not lead to any systematic uncertainties that might depend on the location of the star on the maser mosaic field. In order to evaluate whether this is the case, we have estimated first the deviation of the astrometric and proper motion values of one of the jackknife cases from those in the case in which all seven masers were used. The weighted standard deviations of seven cases were then calculated and plotted as color maps in Figure 6. The positions in the epoch 2000.0 were used for the astrometric comparison in Figure 6.

In Figure 7, the comparisons of IR and radio positions of masers in all seven jackknife cases are shown. The case in which all masers are used is also included in this figure as the "all" case. Each jackknife case agrees with each other, and also with the "include all" case within 1σ, suggesting that the selection of masers should not affect the zero-point of the IR astrometric reference frame. We further investigate how the SMBH parameters may be affected by the maser selection in the next section.

5.3. The Effect of the New Reference Frame on the S0-2 Orbit

Since the IR positions of all stars on the master starlist per epoch are transposed to the radio Sgr A* rest frame, if the perfect reference frame is achieved, the mean position and proper motion of Sgr A* in the IR reference frame should be zero. If not, the orbit of, for example, S0-2 would exhibit a shift resulting in an unclosed orbit, as the zero-point of each coordinate system would systematically wander. For the reference frame being presented in this paper, as seen in

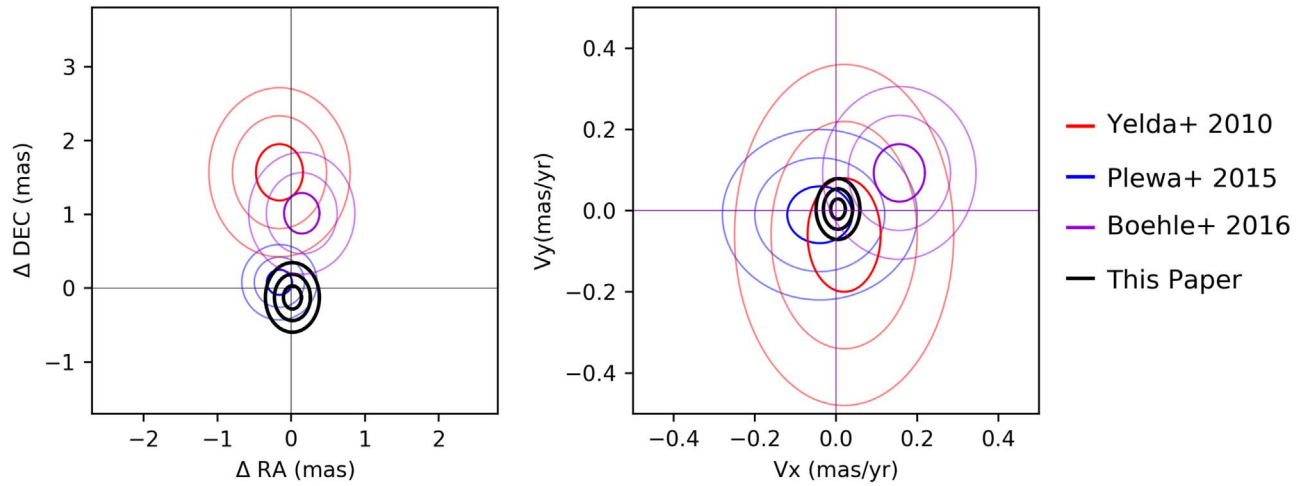

Figure 5. Comparison of the stability of the reference frame as measured by the average differences between the positions and velocities in the radio and IR. The agreements of the maser positions (left) and velocities (right) in the IR are compared to those in the radio. The ellipses represent 1σ, 2σ, and 3σ uncertainties. For the Keck/NIRC2 data, the uncertainty in the distortion correction of 1 mas that dominates the IR error was subtracted so as to show the improvement in the methods used in this paper to construct the reference frame.

Table 3, the agreement between the IR and radio maser positions and proper motions is consistent with zero within uncertainties. The star S0-2 has a period of 16yr, and its positions, spanning the period 1995–2017, are shown in the right panel of Figure 8 after being cross-epoch aligned to the common reference frame (S. Jia et al. 2018, in preparation), with the orbit model fit superposed in black. Plotted in the left panel in the same figure are the astrometric points of S0-2 cross-epoch aligned using the reference frame used in Boehle et al. (2016), with the orbit model fit superposed. The same set of NIRC2 and radial velocity data were used in both orbits shown in Figure 8; the only difference between the two orbits is the reference frame used. With the previous reference frame, the shift in the radial position of S0-2 was roughly 0.75 mas yr^{-1}, which is clearly seen in Figure 8 as the gap in the orbit in the northeast direction from Sgr A*, whereas with the newer current reference frame the same shift is $\sim$0.05 mas yr^{-1}, an order of magnitude better. Since the analysis of Boehle et al. (2016), the speckle holography data have been reanalyzed and updated. The orbit-fitting results shown in this paper utilize the updated newer version (S. Jia et al. 2018, in preparation). However, when estimating the orbit of S0-2 using the previous version of speckle holography data, but using the most current reference frame being presented here, the orbit is much more "closed," similar to the one shown in Figure 8, than the one presented by Boehle et al. (2016), suggesting that the new reference frame plays a larger role in refining the S0-2 orbit than the reanalyzed NIRC2 speckle data.

We further examine how each jackknife reference frame affects the black hole parameters determined from the orbit fitting following the procedure described in detail in Ghez et al. (2005b, 2008) and Boehle et al. (2016). Each jackknife reference frame, as described in the previous section, is used for cross-epoch alignment of central 10″ data, followed by the orbit-fitting procedure for each case to estimate the parameters of the Galactic Center SMBH (see Ghez et al. 2008; Boehle et al. 2016). The case in which no maser is dropped is the same alignment of cross-epoch central 10″ data presented in S. Jia et al. (2018, in preparation). Examining the statistical bias of SMBH parameters using the seven subset reference frames by applying the equations in Appendix C of Boehle et al. (2016), we estimate that the measurements are biased at a 2σ level.

One of the motives for improving the IR reference frame has been the opportunity to be able to test general relativity as S0-2 reached its closest approach to the SMBH in 2018. Furthermore, observations of the apocenter shift of S0-2 should be possible in future, if the uncertainty in the stability of the reference frame of $\sim$0.02 mas yr^{-1} is achieved (Weinberg et al. 2005). Yelda et al. (2010) reported that this stability would not be achieved until $\sim$2022 based on six epochs of maser observations. We are now able to revisit this question with more than twice the amount of data. Figure 9 shows the improvement in the reference frame. It displays the uncertainty in the velocity of Sgr A* in the IR reference frame as a function of time. The trends presented in Yelda et al. (2010) are represented in this figure by dashed lines. By the year 2020, with three additional epochs of maser data starting in 2018, the combined stability of $\sim$0.02 mas yr^{-1}, shown by a gray horizontal line, can be reached.

5.4. Position of Sgr A*

Another method of examining how well the IR astrometric reference frame is determined is to compare the position of Sgr A*-IR on maser mosaic frames with the predicted radio position of Sgr A*. Sgr A*-IR is highly variable (Genzel et al. 2003; Ghez et al. 2004, 2005a; Witzel et al. 2018), and it is not often detectable, especially in short-exposure maser mosaics. However, we make use of the central 10″ data by examining single frames from a given epoch, which allows us to pinpoint the location of Sgr A*-IR when it flares. The position of Sgr A*-IR is then located on the maser mosaic field if the maser and central 10″ observations were taken within approximately a month of each other. Otherwise, the stars closest to the SMBH would have moved far enough that the location of Sgr A*-IR cannot be determined accurately enough. We have examined each epoch of data and found that Sgr A*-IR is visible in three epochs: 2008, 2010, and 2014. The results are shown in Figure 10. The R.A. and decl. positions of Sgr A*-IR in three epochs are shown as a function of time, with the predicted positions and uncertainties determined from the reference

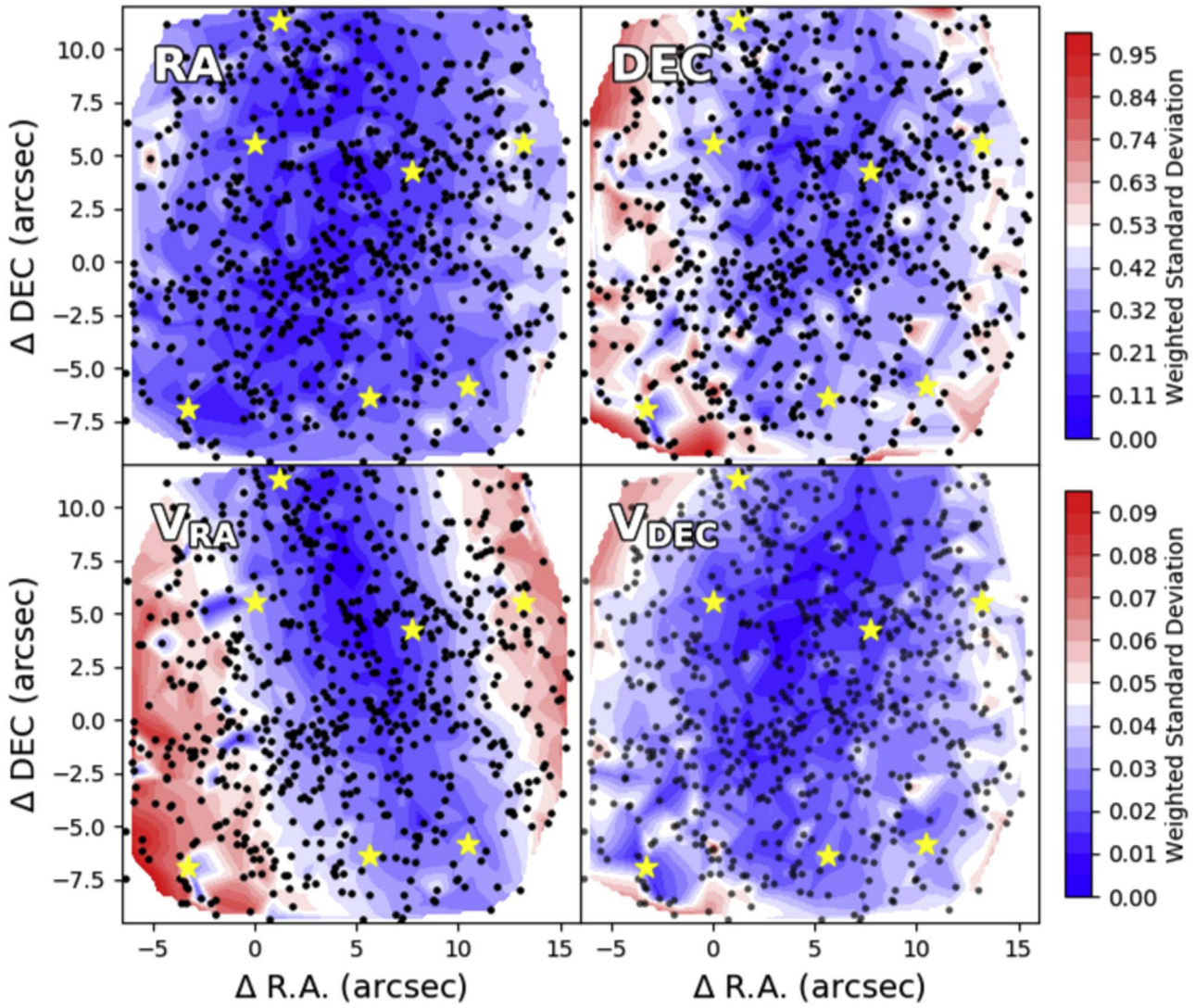

Figure 6. Stability of the stellar positions (top) and velocities (bottom) of the secondary astrometric standard stars as determined from a jackknife bootstrap over the seven masers. The dots show the positions of secondary astrometric stars. The positions of masers are shown by yellow stars. For each star, shifts in the R.A. and decl. positions for the year 2000.0 and $V_{\rm R.A.}$ and $V_{\rm decl.}$ proper motions are calculated as one maser is dropped from the construction of the reference frame, and the weighted standard deviations of seven drop-one-maser cases are calculated and plotted. The shaded color map shows the weighted standard deviations in R.A. (upper left) and decl. (upper right) positions and R.A. (lower left) and decl. (lower right) proper motions.

frame, as shown in Table 3, overplotted. With the exception of the 2014 decl. position, the position of Sgr A*-IR agrees well with the zero-point of the reference frame. Sgr A*-IR is fainter in 2014 than in the other two epochs, which may explain the slight discrepancy.

6. Summary

We have presented an improved astrometric reference frame in the near-IR, which is used for monitoring the positions of stars in the vicinity of Sgr A* to determine the SMBH properties. In the current IR reference frame, the position of Sgr A* is localized within 0.458 mas and 0.455 mas in the east and north directions respectively, and the proper motions within 0.008 mas yr^{-1} and 0.004 mas yr^{-1} in the east and north respectively.

As shown in Section 5, the IR astrometric reference frame still depends slightly on the choice of masers; for example, the IR position of Sgr A* is estimated with bias of 1.9–2.3 mas. The way to decrease this bias may be to include additional masers in the analysis. However, the observation of additional NIRC2 positions is time-consuming, and realistically not viable. There are several *Gaia* sources with proper motion measurements in the Galactic Center region. However, again, they are unfortunately located just outside our maser mosaic field. Multi-epoch observations with the *Hubble Space Telescope* should be able to provide additional stellar positions and proper motion data within the mosaic field. Any stars can be used as reference stars, as long as their proper motions are estimated accurately enough.

We thank the staff of the Keck Observatory, especially Randy Campbell, Jason Chin, Scott Dahm, Heather Hershey, Carolyn Jordan, Marc Kassis, Jim Lyke, Gary Puniwai, Julie Renaud-Kim, Luca Rizzi, Terry Stickel, Hien Tran, Peter Wizinowich, Carlos Alvarez, Greg Doppman and current and former directors, Hilton Lewis and Taft Armandroff, for all their help in obtaining observations. We would also like to thank the anonymous referee for very useful comments and

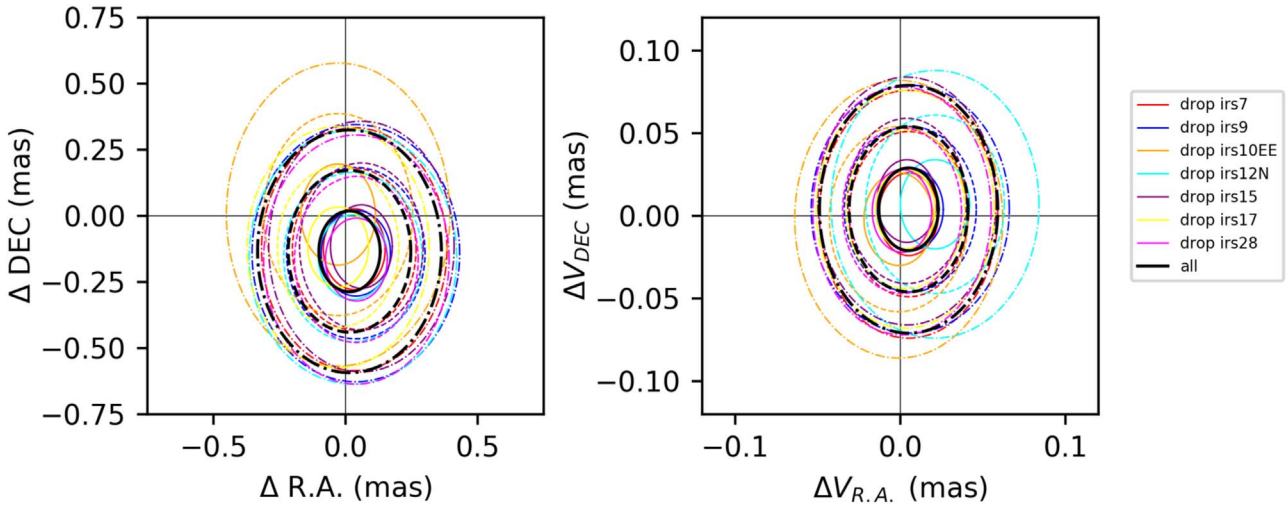

Figure 7. Comparison of the IR reference frame determined for each drop-one-maser case with the radio astrometric reference frame. For each maser dropped, 1σ, 2σ, and 3σ uncertainties are shown. The dropped maser is color-coded following the legend on the right. The radio astrometric coordinate system is based on the assumption that Sgr A* is at (R.A., decl.) = (0, 0) and at rest.

suggestions. Support for this work at UCLA was provided by Heising Simons Foundation (2017-282) and National Science Foundation (AST-1412615). Also, matching funds to The W. M. Keck Foundation (20170668) were provided to UCLA and UC Berkeley. Furthermore, S.J., J.R.L., and M.W.H. acknowledge support from NSF AAG (AST-1518273).

The W. M. Keck Observatory is operated as a scientific partnership among the California Institute of Technology, the University of California, and the National Aeronautics and Space Administration. The Observatory was made possible by the generous financial support of the W. M. Keck Foundation. The authors wish to recognize and acknowledge the very significant cultural role and reverence that the summit of Maunakea has always had within the indigenous Hawaiian community. We are most fortunate to have the opportunity to conduct observations from this mountain.

Facility: Keck Observatory.

Software: astropy (Astropy Collaboration et al. 2013), KS2 (Anderson et al. 2008), Matplotlib (Hunter 2007), SciPy (Jones et al. 2001).

Appendix
Local Distortion Correction

In Yelda et al. (2010), four-parameter fits (X/Y translation, scale, and rotation) were used to mosaic together stellar positions of nine dither images to create one starlist for each epoch. However, we have adopted a third-order polynomial fit in step (1) in Section 2.4 when matching the observed astrometric positions to the master starlist, to accommodate the change in the optical distortion corrections in 2015 (Service et al. 2016), caused by the realignment in the AO system and NIRC2 camera. Before the change in 2015, there was no evidence of time variability in the distortion solution, which captures the geometric optical distortions and likely some PSF variation over the field. Service et al. (2016) only had one year of time sampling and the distortion seemed constant within the uncertainties. However, we have subsequently found that there are time-dependent variations in the distortions beyond 2015. This is apparent in the central 10″ pointings of the Galactic Center data, which are always taken at the exact same sky options. We do not have enough data to determine whether the distortion pattern is drifting slowly or is changing more randomly. Thus we are unable to construct a "master" distortion map for all epochs.

The details of deriving the local distortion correction for the central 10″ field are presented in S. Jia et al. (2018, in preparation). Briefly, it is determined from the residuals of the comparison between the observed position for that epoch and the predicted position from the proper motions from the standard NIRC2–LGSAO setup (S. Jia et al. 2018, in preparation). A set of stars with high-accuracy proper motion measurements is required to create the local distortion map. Unfortunately, the local distortion correction for the central 10″ field cannot be applied to the maser mosaic fields, because the correction appears to depend on the position of NIRC2 with respect to the tip–tilt star. The same tip–tilt star is used for the central 10″ and maser mosaic observations. One of the major reasons for needing the local distortion correction is the PSF variation across the NIRC2 field. Since the dither positions of the maser mosaic are all at different locations with respect to the central 10″ field, its PSF variation across the NIRC2 field differs as well. Thus we cannot apply the local distortion correction for the central 10″ derived by S. Jia et al. (2018, in preparation) to the stellar positions of the maser mosaic.

Furthermore, we are unfortunately not able to derive the local distortion correction for maser mosaic fields, since even though more than 700 secondary astrometric stars are found in the entire maser mosaic field, each dither position encompasses less than ∼100 such stars. This is not enough to fit a fourth-order polynomial, which would be needed to fully specify the local distortion correction. Our solution is to compromise with a third-order polynomial fit to combine multiple maser fields together to create a master starlist for each epoch. The residuals after the third-order fit are less than ∼0.1 mas, which is less than the error in the radio maser positions; thus we did not need to go to a higher order than we are currently using. If we used

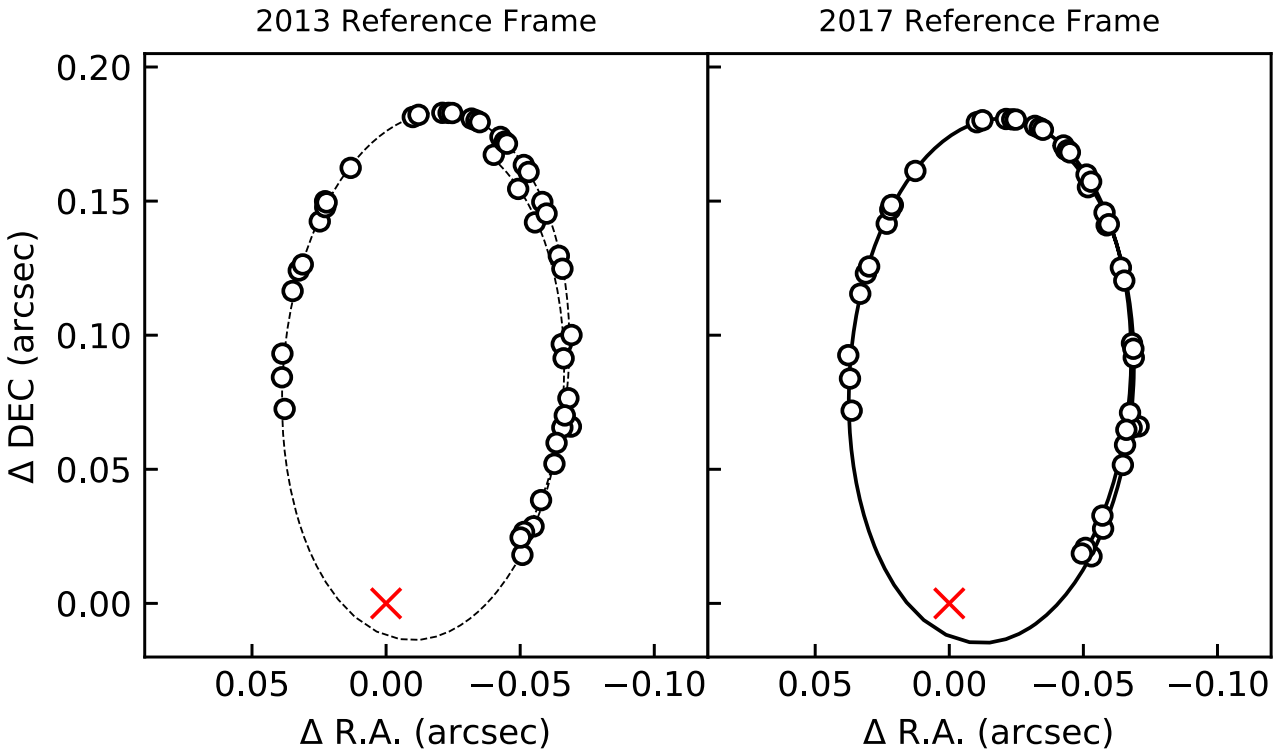

Figure 8. Comparison of S0-2 orbits based on the current IR reference frame presented in this paper (right) with the one presented in Boehle et al. (2016) (left). The position of the black hole is indicated by a red cross.

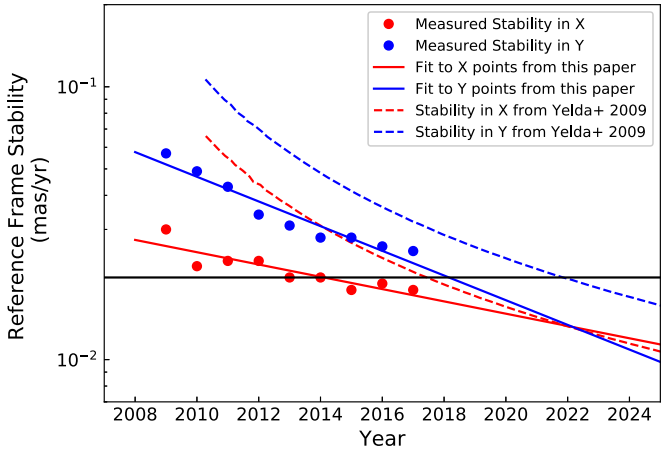

Figure 9. The improvement in the stability of the reference frame as a function of time, which corresponds to the number of epochs of observations. We have obtained one set of maser observations every year starting in 2005. As of 2017, 13 epochs of observations in IR have been made. The figure shows the stability of the reference frame determined for each epoch, using maser observations up to and including that epoch. For future points, it is assumed that one set of maser observations is taken every year. The actual observed errors in X and Y proper motion are represented by red and blue solid circles respectively. The solid lines show the fits through the observed data points, while the dashed lines show the predictions from Yelda et al. (2010). The gray horizontal line shows the uncertainty that needs to be achieved in order to observe the apocenter shift of S0-2.

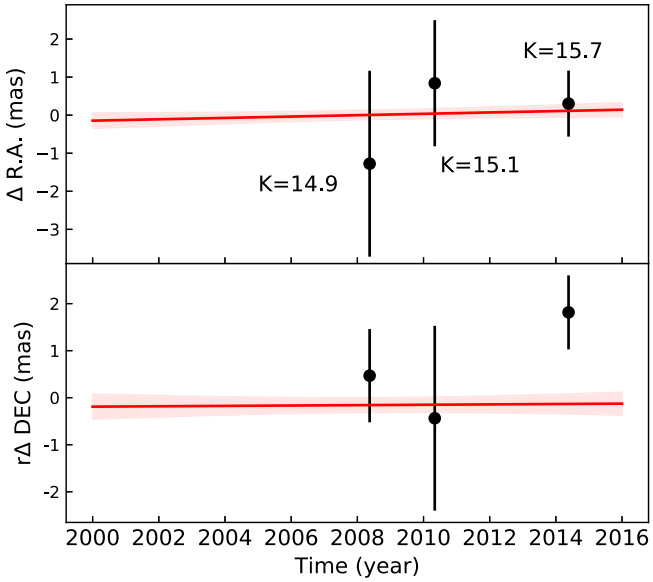

Figure 10. R.A. and decl. positions of Sgr A*-IR as detected in the maser mosaic image. The red line shows the predicted positions and uncertainties determined from the reference frame as shown in Table 3.

the second-order parameter fit, as was done in Yelda et al. (2010), the post-2015 IR positions would appear significantly further away from the radio positions. The median values of the geometric distortion correction are around 0.01 and −0.03 pixels in X and Y respectively before 2015 (Yelda et al. 2010) and −0.09 and 0.05 after 2015 (Service et al. 2016), while the median values of the local distortion corrections are in the range of 0.02–0.05 pixels (0.2–0.5 mas) with uncertainties around 0.01–0.04 pixels (0.1–0.4 mas). These are relatively smaller than other sources of uncertainty discussed above.

ORCID iDs

Shoko Sakai https://orcid.org/0000-0001-5972-663X
Jessica R. Lu https://orcid.org/0000-0001-9611-0009
Siyao Jia https://orcid.org/0000-0001-5341-0765
Tuan Do https://orcid.org/0000-0001-9554-6062
Gunther Witzel https://orcid.org/0000-0003-2618-797X
Abhimat K. Gautam https://orcid.org/0000-0002-2836-117X
M. W. Hosek, Jr. https://orcid.org/0000-0003-2874-1196

References

Anderson, J., Sarajedini, A., Bedin, L. R., et al. 2008, AJ, 135, 2055
Astropy Collaboration, Robitaille, T. P., Tollerud, E. J., et al. 2013, A&A, 558, A33
Boehle, A., Ghez, A. M., Schödel, R., et al. 2016, ApJ, 830, 17
Danchi, W. C., Bester, M., Degiacomi, C. G., et al. 1994, AJ, 107, 1469
Diolaiti, E., Bendinelli, O., Bonaccini, D., et al. 2000, adass IX, 216, 623
Genzel, R., Schödel, R., Ott, T., et al. 2003, Natur, 425, 934
Ghez, A. M., Hornstein, S. D., Lu, J. R., et al. 2005a, ApJ, 635, 1087
Ghez, A. M., Salim, S., Hornstein, S. D., et al. 2005b, ApJ, 620, 744
Ghez, A. M., Salim, S., Weinberg, N. N., et al. 2008, ApJ, 689, 1044
Ghez, A. M., Wright, S. A., Matthews, K., et al. 2004, ApJL, 601, L159
Gillessen, S., Eisenhauer, F., Trippe, S., et al. 2009, ApJ, 692, 1075
Gravity Collaboration, Abuter, R., Amorim, A., et al. 2018, A&A, 615, L15
Hunter, J. D. 2007, CSE, 9, 90
Jones, E., Oliphant, T., Peterson, P., et al. 2001, SciPy: Open Source Scientific Tools for Python, http://www.scipy.org/
Menten, K. M., Reid, M. J., Eckart, A., & Genzel, R. 1997, ApJL, 475, L111
Ohnaka, K., Bergeat, J., & Driebe, T. 2005, A&A, 429, 1057
Perrin, G., Cotton, W. D., Millan-Gabet, R., & Mennesson, b. 2015, A&A, 576, A70
Plewa, P. M., Gillessen, S., Eisenhauer, F., et al. 2015, MNRAS, 453, 3234
Pott, J.-U., Eckert, A., Glindemann, A., et al. 2008, A&A, 487, 413
Reid, M. J., & Brunthaler, A. 2004, ApJ, 616, 872
Reid, M. J., Menten, K. M., Genzel, R., et al. 2003, ApJ, 587, 208
Reid, M. J., Menten, K. M., Trippe, S., Ott, T., & Genzel, R. 2007, ApJ, 659, 378
Service, M., Lu, J. R., Campbell, R., et al. 2016, PASP, 128, 095004
van Dam, M. A., Bouchez, A. H., Le Mignant, D., et al. 2006, PASP, 118, 310
Weinberg, N. N., Milosavljević, M., & Ghez, A. M. 2005, in ASP Conf. Ser. 338, Astrometry in the Age of the Next Generation of Large Telescopes, ed. P. K. Seidelmann & A. K. B. Monet (San Francisco, CA: ASP), 252
Wittkowski, M., Boboltz, D. A., Ohnaka, K., Driebe, T., & Scholz, M. 2007, A&A, 470, 191
Witzel, G., Lu, J. R., Ghez, A. M., et al. 2016, Proc. SPIE, 9909, 99091O
Witzel, G., Martinez, G., Hora, J., et al. 2018, ApJ, 863, 15
Wizinowich, P. L., Le Mignant, D., Bouchez, A. H., et al. 2006, PASP, 118, 297
Yelda, S., Ghez, A. M., Lu, J. R., et al. 2014, ApJ, 783, 131
Yelda, S., Lu, J. R., Ghez, A. M., et al. 2010, ApJ, 725, 331